J. Fluid Mech. (2013), *vol.* 730, *pp.* 533–558.
doi:10.1017/jfm.2013.360

The decay of the flow in the end region of a suddenly blocked pipe

Nathaniel Jewell[1] **and James P. Denier**[2],†

[1]School of Mathematical Sciences, The University of Adelaide, Adelaide 5005, Australia

[2]Department of Engineering Science, The University of Auckland, Auckland 1142, New Zealand

(Received 1 August 2012; revised 9 May 2013; accepted 11 July 2013;
first published online 7 August 2013)

We consider the decay to rest of initially laminar flow within the end region of a suddenly blocked pipe. Here the flow is dominated by two temporally developing boundary layers, one on the pipe wall and one located at the blockage. The evolution and interaction of these boundary layers contributes to the creation and annihilation of toroidal vortices in the end-region flow, the number and extent growing with increasing Reynolds numbers. For larger Reynolds numbers, these nonlinear vortices delay the decay process within the end region, decaying at a slower rate than flow far downstream of the blockage. Our numerical simulations for pre-blockage Reynolds numbers up to 3000 indicate that the flow in this end region is stable to axisymmetric disturbances.

Key words: boundary layers, boundary layer structure, pipe flow boundary layer

1. Introduction

Fluid flows which are suddenly decelerated arise in many areas of fluid mechanics. Flows in which that sudden deceleration is due to the imposition of a blockage have important applications across a wide range of disciplines. Although there are many such examples, two of particular interest are the flow which occurs when a valve is suddenly closed in a pipe, or pipe network, and that of the rhythmic opening and closing of valves in the human body. The latter example is most readily seen in the behaviour of the *aortic valve* and the *pulmonic valve* in the heart during ventricular ejection. Both of these applications have as their hallmark the fact that the unsteady flow that develops as a result of the sudden change to the flow state exhibits a transient turbulent state; the physiological applications are well represented by the works of Seed & Wood (1971), Nerem & Seed (1972) and Sugawara (1987) and the pipe flow applications by the work of Das & Arakeri (1998).

In the case of a simple pipe flow which is suddenly blocked by a valve, the flow downstream of the blockage can be described by a simple diffusion equation with a source term that represents the unsteady (decaying) streamwise pressure gradient within the flow. Weinbaum & Parker (1975) were the first to consider this problem, giving it its correct mathematical formulation and providing solutions for the decaying flow based upon the Pohlhausen method, used extensively in the early days of boundary-layer research (Schlichting 1979). Their analysis of the decaying streamwise

† Email address for correspondence: j.denier@auckland.ac.nz

(or axial) flow demonstrated that the flow develops points of inflection, thus suggesting that the flow may be susceptible to wave-like instabilities. Subsequent work by Hall & Parker (1976) on the stability of the flow in a suddenly blocked channel, who employed a WKBJ-style approximation based upon the assumption of large flow Reynolds number to derive a quasi-steady Orr–Sommerfeld equation, suggested a minimal critical Reynolds number of 148.2 at the non-dimensional time $t = 0.023$.

The result that the decelerating flow in a suddenly blocked channel (or pipe) is unstable to wave-like disturbances is in qualitative agreement with *in vivo* measurements of turbulence levels in the ascending aorta (Seed & Wood 1971; Nerem & Seed 1972; Sugawara 1987). Hall & Parker (1976) demonstrated that the decaying flow within a suddenly blocked channel is unstable, as a result of the development the inflection points in the streamwise velocity, for Reynolds numbers as low as $O(10^2)$. Of course, some care must be taken in interpreting these results, since the quasi-steady approximation requires the mathematically mutually exclusive requirements on the Reynolds number to be both sufficiently large (indeed, asymptotically large) for the asymptotic approximation to be valid and finite in order to justify retaining viscous terms in the resulting Orr–Sommerfeld equation.

A major driver in the renewed interest in the behaviour of the suddenly blocked pipe flows comes from the water utility industry, where considerable attention has been directed at developing non-invasive techniques to detect leaks in pipeline systems; one such collection of techniques are the so-called *inverse transients*: see Liggett & Chen (1994) for details. For this technique to be fully implemented it is necessary to be able to differentiate between damping due to leaks and damping due to the typically turbulent flow within the pipe (or most often, pipeline). Existing models of unsteady friction, such as those of Brunone, Golia & Greco (1991) and Vardy & Brown (1995), are empirical, typically under-predicting both the amplitude and speed of the resulting pressure wave when the pipe (or pipeline) is subjected to a short-time transient event. There is a considerable body of literature reporting on experiments, conducted largely within copper pipes, which have produced significant data on the pressure at points within the flow. The results presented by Lambert *et al.* (2001) support the conjecture that the observed discrepancy between experiments and the results predicted by theory is largely due to the empirical nature of the friction models. Their experiments were conducted in a copper pipe with the result that their data, used for comparison with steady friction models, was restricted to pressure measurements at the location of the blockage. Lambert *et al.* (2001) suggested a new model for one-dimensional turbulent unsteady friction based upon the growth of the wall boundary layer during the transient events. Their results, derived assuming steady boundary-layer growth, showed some improvements over the classical empirical models in predicting the decay in amplitude of the pressure, and provided a better match for pressure wave speed. Further experiments may, of course, provide improvements in such prediction but a coherent theory based upon flow physics remains elusive. Furthermore, there seems to be little compelling evidence to suggest that the flow is in a fully developed turbulent state throughout the transient event.

This realization has led to a number of studies on the stability of unsteady decaying flows in pipe, ranging from those which exploit a quasi-steady approximation (Hall & Parker 1976; Das & Arakeri 1998; Ghidaoui & Kolyshkin 2001, 2002) to those exploiting a transient growth analysis (Jewell & Denier 2006; Jewell 2009). These works, which provide some qualitative agreement with available experiments (see Das & Arakeri (1998) for example and the more recent experiments of Nishihara *et al.* (2009, 2010) and Sengi *et al.* (2011)) fail to take into account the important region of

the flow in the vicinity of the blockage. Experiments reported by Toophanpour-Rami *et al.* (2007) suggest that a complicated unsteady flow develops in the vicinity of the blockage and that this region may become unstable before the region away from the blockage. Peixinho (private communication) has shown that for moderate Reynolds numbers the instability appears to be related to that described in the transient analysis of Jewell & Denier (2006), whereas for higher Reynolds number the instability may possibly propagate along the pipe from the blockage region.

The end region is also important if we are to develop a fuller understanding of the multiple-wave reflection events that occur in suddenly blocked flows. It may well be that the vorticity within the flow prior to the reflection of the pressure wave that arises from the sudden blockage can be approximated by that due to the decaying streamwise flow $u(r, T)$ of § 2. If this is the case then the analysis of Weinbaum & Parker (1975) and Jewell & Denier (2006) can be repeated to determine the subsequent sequence of wave reflections and the decaying friction within pipelines. This appears to be the procedure adopted by Ghidaoui & Mansour (2002), who present results for the streamwise velocity profile after the first passage of the reflected pressure wave (their figure 3); see also Nishihara *et al.* (2009, 2010) and Sengi *et al.* (2011). However, this procedure ignores the presence of the blockage region, focusing solely upon the flow downstream of the blockage.

Our understanding of this blockage region, how it develops, its stability and how ultimately it decays, is lacking. This paper is a first step towards understanding the dynamics of this region of the flow. After some preliminary formulation in § 2, we describe the salient features of our numerical treatment of the problem in § 3; a small-time solution to the full (axisymmetric) Navier–Stokes equations which provides the initial condition for our numerical integration is detailed in an Appendix. The results of our calculations are presented in § 4, and finally in § 5 we present some conclusions and directions for future work.

2. Formulation

Consider the fully developed uni-directional flow of a viscous incompressible fluid of density ρ and kinematic viscosity ν flowing in a cylindrical pipe of radius $R = R^*$. Let (u, v, w) denote the dimensionless velocity, non-dimensionalized with respect to the centreline axial velocity, in non-dimensionalized cylindrical polar coordinates (x, r, θ). The fully developed flow is then Hagen–Poiseuille flow, in which

$$(u, v, w) = (1 - r^2, 0, 0), \tag{2.1}$$

where $r = 1$ denotes the non-dimensionalized pipe radius. Now suppose that at time $t = 0$ the flow is suddenly blocked at some streamwise location, which we will take to be $x = 0$. The net flow $\bar{u}$ through the pipe is reduced impulsively to zero, but the fluid itself takes an appreciable time to come to rest. The resulting transient laminar flow $\boldsymbol{u}(r, x > 0, t > 0)$ constitutes the subject of this paper.

Some progress on this problem was made by Weinbaum & Parker (1975). They demonstrated that the flow vorticity is effectively frozen during the passage of the initial, impulsive pressure wave. Thus, provided the Mach number of the flow is small (as it is in most pipeline applications involving liquids), the vorticity distribution immediately following the blockage event ($t = 0^+$) is given by $\boldsymbol{\omega} = 2r$. By solving the vorticity equation, Weinbaum & Parker (1975) derived the instantaneous

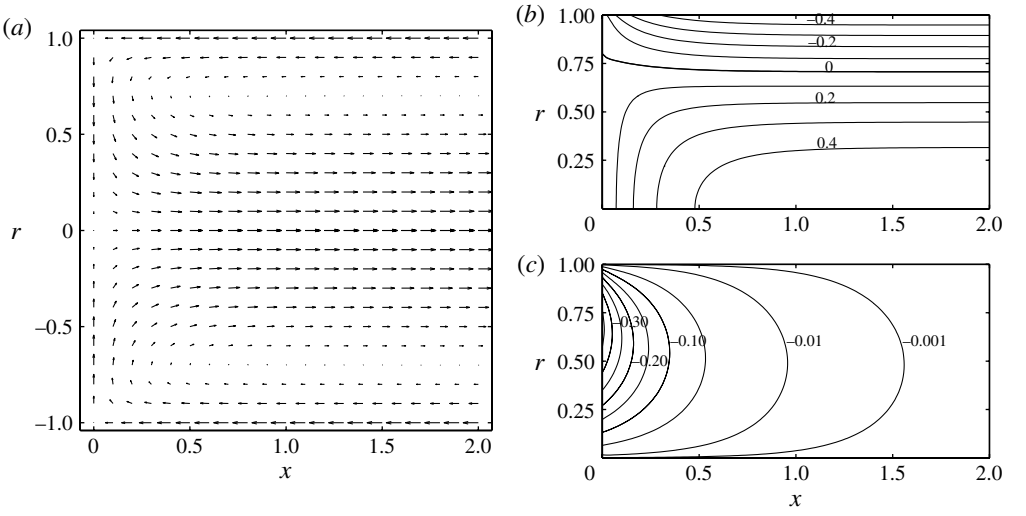

FIGURE 1. The flow field at time $t = 0^+$, immediately following the blockage event but before the flow has had time to adjust to the no-slip boundary conditions. (*a*) Full-diameter quiver plot ($-1 \leqslant r \leqslant 1$) of the $t = 0^+$ flow. (*b*) Semi-diameter contour plot ($0 \leqslant r \leqslant 1$) of the streamwise velocity u. (*c*) Semi-diameter contour plot of radial velocity v.

velocity $\boldsymbol{u}(r, x, 0^+)$ in the form

$$\psi_0(r, x) = \frac{1}{4} r^2(1 - r^2) - 4 \sum_{n=1}^{\infty} \left[\frac{\lambda_n^{-3}}{\mathrm{J}_2(\lambda_n)} \right] r \mathrm{J}_1(\lambda_n r) \exp(-\lambda_n |x|), \tag{2.2}$$

where

$$u = \frac{1}{r} \frac{\partial \psi_0}{\partial r} \quad \text{and} \quad v = -\frac{1}{r} \frac{\partial \psi_0}{\partial x}, \tag{2.3}$$

J_1 and J_2 are the Bessel functions of the first and second kind respectively, and $\{\lambda_n, n = 1, 2, \ldots\}$ are the zeros of $\mathrm{J}_1(x)$ (see Abramowitz & Stegun 1965). This profile comprises a core forward flow ($u > 0$ for $0 \leqslant r < 0.707$) balanced by reversed flow near the pipe sidewall ($u < 0$ for $0.707 < r \leqslant 1$). This instantaneous ($t = 0^+$) velocity field is plotted in figure 1. Note that free-slip conditions apply on the walls ($u = -1/2$ at $r = 1$ for $x > 00$; $v < 0$ at $x = 0$ for $0 < r < 1$), since insufficient time has elapsed for the development of viscous boundary layers. It follows from (2.2) that the flow at $t = 0^+$ approaches its upstream limit *exponentially* in the streamwise coordinate:

$$(u_0, v_0) = (\tfrac{1}{2} - r^2, 0) + O(e^{-\lambda x}) \quad \text{for } x \gtrsim 1, \tag{2.4}$$

where $\lambda = \lambda_1 \approx 3.83$.

We now consider how the flow subsequently decays to rest for $t > 0$ (as it must in the absence of an imposed pressure gradient). We first note that the diffusion time scale is $T = Re^{-1}t$. The early-decay phase ($T \ll 1$) is characterized by the development of viscous boundary layers at $r = 1$ and $x = 0$, which allow the flow to adjust to the full no-slip conditions on the pipe wall and at the blockage. We assume that the flow remains laminar and axisymmetric throughout the decay process, and thus may be represented by a single unsteady streamfunction $\psi(r, x, T)$. The Navier–Stokes

equations then reduce to

$$\frac{\partial}{\partial T}(\widetilde{\nabla}^2\psi) + Re(r^{-1}\psi_r\widetilde{\nabla}^2(\psi_x) - r^{-1}\psi_x\widetilde{\nabla}^3\psi) = \widetilde{\nabla}^4\psi, \tag{2.5a}$$

where the following differential operators have been introduced:

$$\widetilde{\nabla}^3 \equiv \frac{\partial^3}{\partial r^3} + \left(\frac{\partial}{\partial r} - \frac{2}{r}\right)\frac{\partial^2}{\partial x^2} - \frac{3}{r}\left(\frac{\partial^2}{\partial r^2} - \frac{1}{r}\frac{\partial}{\partial r}\right), \tag{2.5b}$$

$$\widetilde{\nabla}^4 \equiv \frac{\partial^4}{\partial x^4} + 2\left(\frac{\partial^2}{\partial r^2} - \frac{1}{r}\frac{\partial}{\partial r}\right)\frac{\partial^2}{\partial x^2} + D_r^4, \tag{2.5c}$$

$$D_r^4 \equiv \frac{\partial^4}{\partial r^4} - \frac{2}{r}\frac{\partial^3}{\partial r^3} + \frac{3}{r^2}\left(\frac{\partial^2}{\partial r^2} - \frac{1}{r}\frac{\partial}{\partial r}\right). \tag{2.5d}$$

The boundary conditions on the streamfunction are

$$\psi = 0 \quad \text{and} \quad \psi_{\boldsymbol{n}} = 0 \quad \text{at } x = 0 \text{ and } r = 1, \tag{2.6}$$

together with suitable far-field x-wise boundary conditions; here a subscript $\boldsymbol{n}$ denotes differentiation in the direction normal to the solid boundary. We will return to a discussion of these shortly when we come to discuss the numerical scheme that will be used to solve (2.5).

Well downstream of the blockage location, the decaying flow is unidirectional and takes the form

$$\boldsymbol{u}(r, x, T) = (u(r, T), 0, 0) \quad \text{for } x \gg 1. \tag{2.7}$$

This problem was first considered by Weinbaum & Parker (1975) and revisited by Jewell & Denier (2006). Accordingly, our primary interest here is with the decay of the flow in the immediate vicinity of the blockage, corresponding to $x = O(1)$. It is nevertheless instructive to review the upstream flow $u(r, T)$, since it exhibits salient features of the full blockage-region flow and will be incorporated into our numerical scheme.

Weinbaum & Parker (1975) demonstrated that the upstream flow is planar and governed by the diffusion equation

$$\frac{\partial u}{\partial T} = \phi'(T) + \frac{\partial^2 u}{\partial r^2} + \frac{1}{r}\frac{\partial u}{\partial r}, \tag{2.8a}$$

where $T = Re^{-1}t$ and $\phi'(T)$ denotes the (temporally) decaying streamwise pressure gradient due to a secondary pressure wave. This equation must be solved subject to the initial and boundary conditions

$$u(r) = \tfrac{1}{2} - r^2, \quad \text{at } T = 0, \tag{2.8b}$$

$$u(1) = 0 \quad \text{for } T > 0, \tag{2.8c}$$

and a zero-net-flux condition across the pipe:

$$\int_0^1 u(r, T) r \, \mathrm{d}r = 0. \tag{2.8d}$$

The impulsive nature of this flow is reflected in the development of a boundary layer at $r = 1$ of non-dimensional thickness $\delta = O(\sqrt{T})$. This, coupled with the constraint of zero net flow, induces a square-root singularity $\phi' = O(T^{-1/2})$ as $T \to 0^+$ in

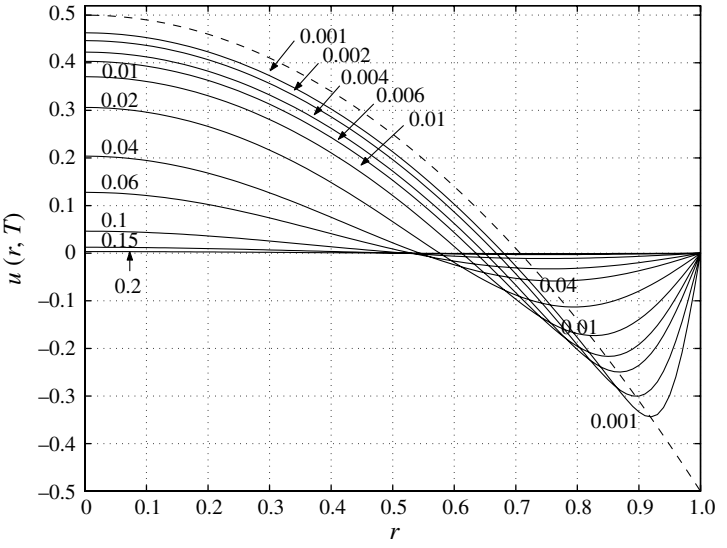

FIGURE 2. Plot of streamwise velocity $u(r, T)$ versus r for times T as indicated. The dashed curve shows the inviscid $T = 0$ solution.

the decaying streamwise pressure gradient. To address this computational challenge, Weinbaum & Parker (1975) employed an approximate Pohlhausen method to develop solutions to (2.8). Recently, in the context of a study of the linear stability of the flow downstream of the blockage, Jewell & Denier (2006) solved (2.8) by first developing a uniformly valid small-T solution. Their semi-analytic expression remains accurate until $T \approx 0.05$ (at which time the axisymmetric boundary layer nearly fills the pipe); this approach furnished initial conditions at time $T_0 = O(10^{-2})$ for a Crank–Nicolson scheme which evolved the solution forward until the flow became vanishingly small ($T_{max} \approx 0.2$). The important feature of this flow, first identified by Weinbaum & Parker (1975), is the presence of an appreciable region of reversed flow ($u < 0$) at the pipe wall: see figure 2.

In the region adjacent to the blockage, the flow is governed by the full Navier–Stokes equations (2.5) with which little analytical progress can be made, and so a numerical treatment is required. As was the case for the flow downstream of the blockage, considered in Jewell & Denier (2006), we must supply appropriate initial conditions at some small, but non-zero, time T_0 in order to overcome the singularity at $T = 0$ which arises due to the impulsive nature of the blockage flow. The details of the small-time structure of the flow are presented in the Appendix; we will discuss the salient details of this small-time solution as it applies to the initial condition to be used in our full simulations.

3. The numerical scheme

We now turn our attention to the numerical scheme used to solve the governing equations (2.5) for the unsteady axisymmetric flow in the vicinity of the blockage. The computational domain is defined by

$$\mathscr{D} = \{(x, r) : 0 \leqslant x \leqslant x_{max}, 0 \leqslant r \leqslant 1\}, \tag{3.1}$$

where $x = 0$ corresponds to the position of the blockage (see figure 15) and $x_{max} \approx 5$ is a computational parameter chosen suitably large so as to ensure appropriate matching with the far field. The streamfunction formulation (2.5) is fourth-order and nonlinear; nonetheless, it is computationally attractive in as much as it is self-contained and yields straightforward boundary conditions on the pipe walls and blockage, namely

$$\psi = 0 \quad \text{and} \quad \psi_{\boldsymbol{n}} = 0 \quad \text{at } x = 0, r = 1, \tag{3.2}$$

where $\boldsymbol{n}$ indicates the derivative in the direction normal to the surface.

3.1. *Spatial discretization*

It is expedient to represent the streamfunction ψ in the form

$$\psi(r, x, T) = r^2(1 - r^2)\Psi(r, x, T), \tag{3.3}$$

subject to the single radial boundary condition $\Psi = 0$ at $r = 1$. The local component $\widetilde{\psi}$ of the streamfunction is discretized over the rectangular domain $\mathscr{D}$ of (3.1) using a hybrid Chebyshev–Laguerre pseudospectral scheme. Following Fornberg (1996) and Trefethen (2000), we first extend the radial domain to $-1 \leqslant r \leqslant 1$ and apply a Chebyshev pseudospectral scheme of polynomial order $\approx 2M$, before exploiting radial symmetry to halve the number of flow unknowns to $\approx M$ per x-station. Following Shen (1997, 2000), we discretize the streamwise coordinate x using a pseudospectral scheme constructed from scaled Laguerre functions $\{L_n(kx)\}_{n=0}^{N}$ with $k \gg 1$. Each (unscaled) Laguerre function $L_n(x)$ is defined over the domain $[0, \infty)$ and decays to zero exponentially as $x \to \infty$, but takes order-one values throughout the interval $0 < x \leqslant O(n)$. Thus, the natural collocation points $\{\widetilde{x}_n\}$ of the scaled Laguerre scheme are all finite and non-negative, the largest being $\widetilde{x}_N = O(N/k)$. We therefore choose $k = O(N/x_{max})$ so that $\widetilde{x}_N$ coincides with a suitable value of x_{max}. Typically we found $x_{max} = 5$ adequate to yield domain-independent results, even at the highest Reynolds numbers considered here. Note that this Chebyshev–Laguerre discretization automatically satisfies the asymptotic boundary condition $\widetilde{\psi} \to 0$ as $x \to \infty$, and no explicit boundary conditions are required at the far-field boundary $x = x_{max}$ (which is treated as an ordinary x-wise station). Compared with an all-Chebyshev scheme, our scheme avoids any (computationally wasteful) clustering of collocation points near the artificial far-field boundary $x = x_{max}$ while preserving (desirable) mesh-clustering within the boundary layers on the sidewall $r = 1$ and end-wall $x = 0$.

Our Chebyshev–Laguerre discretization is employed not only for the simulation *per se*, but also for implementation of the small-T initialization routine of § 3.4. The Chebyshev–Laguerre scheme as described above, however, is scarcely adequate for resolving the thin boundary layers observed at $T_0 = O(10^{-4})$. For $T_0 \leqslant T \lesssim 0.01$, therefore, we implement the Chebyshev–Laguerre scheme in (ρ, ξ) space, where $(r, x) \Rightarrow (\rho, \xi)$ is a coordinate bijection of the form

$$0 \leqslant \rho(r) \leqslant r \leqslant 1 \quad \text{with equality iff } r = 0 \text{ or } r = 1, \tag{3.4a}$$

$$0 \leqslant x \leqslant \xi(x) \leqslant x_{max} \quad \text{with equality iff } x = 0 \text{ or } x = x_{max}. \tag{3.4b}$$

For this purpose we use the mapping functions

$$\frac{\xi(x)}{x_{max}} = \frac{\log[1 + a(x/x_{max})]}{\log(1 + a)}, \tag{3.5a}$$

$$\rho(r) = \frac{\log[1 + b(1 + r)] - \log[1 + b(1 - r)]}{\log(1 + 2b)}, \tag{3.5b}$$

where the stretch parameters $a > 0$ and $b > 0$ are reduced gradually to zero across the early phase of simulation ($T_0 \leqslant T \lesssim 0.01$). Conversely, for $T \gtrsim 0.01$ the standard Chebyshev–Laguerre scheme provides sufficient resolution of both boundary layer and internal features of the flow.

3.2. *Temporal discretization*

The streamfunction is initialized at time $T_0 = O(10^{-4})$ from the semi-analytic small-T expansion derived in the Appendix. Time-stepping is performed using the (second-order accurate in time) predictor–corrector method, treating the linear terms implicitly and the advection terms explicitly. Each time step entails two matrix inversions of the form

$$\mathscr{A}\widehat{\psi}^{n+1} = \mathscr{B}_1\psi^n + \mathscr{B}_2\psi^n, \tag{3.6a}$$

$$\mathscr{A}\psi^{n+1} = \mathscr{B}_1\psi^n + \tfrac{1}{2}(\mathscr{B}_2\psi^n + \mathscr{B}_2\widehat{\psi}^{n+1}), \tag{3.6b}$$

where

$$\mathscr{A} = \mathrm{Har} - \frac{\Delta T}{2}\mathrm{Bih}, \quad \mathscr{B}_1 = \mathrm{Har} + \frac{\Delta T}{2}\mathrm{Bih}, \quad \mathscr{B}_2 = (Re)(\Delta T)\mathrm{Adv}, \tag{3.7}$$

and Har, Bih and Adv denote harmonic, biharmonic (diffusion) and nonlinear (advective) operators respectively. The resulting matrix equation is solved at each time step using standard Gaussian elimination, at a computational cost of $O(M^3N^3)$. Full details of the numerical scheme can be found in Jewell (2009, chapter 9).

3.3. *Initial conditions: the small-time solution*

The small-time structure of the flow, presented in the Appendix, demonstrates the singular nature of the flow at time $t = 0$. It also demonstrates that the flow domain can be resolved into four separation subregions; a *wall boundary layer* (see § A.1), a *blockage boundary layer* (see § A.2), a *corner boundary layer* (see § A.3) and the inviscid core-flow, discussed earlier (see figure 15). Although the equations governing the flow within the two wall boundary layers admit analytical solutions, the corner region governed by (A 10) does not, and so must be solved numerically. This in turn poses special challenges in matching the sub-zone solutions. Therefore, instead of solving for all four asymptotic regions separately and then attempting to match the respective solutions, we choose to develop a *composite numerical solution*, informed by the asymptotic structure detailed in the Appendix, for the small-time structure of the streamfunction ψ.

Accordingly, we now reformulate the full problem in terms of the streamfunction ψ. The analysis will be accurate only to leading order at $T = o(Re^{-1})$, and we will not attempt to derive explicit intermediate expressions for the overlap regions in figure 15. We note, however, that the leading-order error-function solution in the wall boundary layer (A 4) for $\eta = O(1)$ decays exponentially into the core-flow; consequently, an intermediate expansion is superfluous, and the edge of the boundary layer can be adequately approximated by $\eta^* \approx 2$ for computational purposes. Similarly, for computational purposes the edge of the blockage boundary layer can be adequately approximated by $\xi^* \approx 2$. Here

$$\eta = \frac{(1-r)}{2\sqrt{T}} \quad \text{and} \quad \xi = \frac{x}{2\sqrt{T}} \tag{3.8}$$

are the wall boundary layer and blockage boundary layer variables respectively (see the Appendix for full details). We note that the values of η^* and ξ^* were chosen

after some experimentation; our results are independent of these choices of $\eta^* \geqslant 2$ and $\xi^* \geqslant 2$.

For our computational purposes, it also proves convenient to subtract the upstream flow component (2.7) from the end-region flow. We therefore rewrite ψ in the form

$$\psi(r, x, T) = \widetilde{\psi}(r, x, T) + \psi_\infty(r, T), \tag{3.9}$$

where, by definition, the tilde quantity satisfies

$$\widetilde{\psi}(r, x, T) \to 0 \quad \text{as } x \to \infty, \tag{3.10}$$

and ψ_∞ corresponds to the upstream component analysed in Jewell & Denier (2006). Led by the analysis presented in the Appendix, we are now in a position to write down the equations that collectively govern the structure of the small-time solution of the flow. It is these equations that must be solved so as to provide the necessary small (but non-zero) initial condition for our full calculations.

3.3.1. *The core region in which* $r, x = O(1)$

The core-region flow is effectively inviscid. The modified streamfunction $\widetilde{\psi}$ satisfies

$$\frac{\partial^2 \widetilde{\psi}}{\partial x^2} + \frac{\partial^2 \widetilde{\psi}}{\partial r^2} - \frac{1}{r}\frac{\partial \widetilde{\psi}}{\partial r} = 0 \quad \text{for } (\eta, \xi) > (\eta^*, \xi^*), \tag{3.11a}$$

and its natural boundary conditions are the free-slip, no-penetration conditions

$$\widetilde{\psi}_r = 0 \quad \text{on } x = 0, \quad \widetilde{\psi}_x = 0 \quad \text{on } r = 1, \tag{3.12}$$

together with the asymptotic condition $\widetilde{\psi} \to 0$ as $x \to \infty$. In practice, however, the boundary conditions will be replaced by boundary-layer matching conditions, while the asymptotic condition will be satisfied automatically by our numerical scheme.

3.3.2. *The blockage boundary layer*

Within the blockage boundary layer for $\xi = O(1)$, the modified streamfunction is governed by the fourth-order linear equation

$$\frac{\partial^4 \widetilde{\psi}}{\partial \xi^4} + 2\xi \frac{\partial^3 \widetilde{\psi}}{\partial \xi^3} = 0 \quad \text{for } 0 < \xi < \xi^*(\eta > \eta^*), \tag{3.11b}$$

subject to boundary conditions

$$\widetilde{\psi} = -\psi_\infty, \quad \widetilde{\psi}_\xi = 0 \quad \text{on } \xi = 0. \tag{3.11c}$$

The remaining two boundary conditions are specified and solved implicitly, by matching with the core-flow solution obtained from (3.11*a*). Thus, the entire end-region flow is scaled by the inhomogeneous boundary condition in (3.11*c*), together with those of (3.11*f*) and (3.11*g*) given below for the corner boundary layer.

3.3.3. *The wall boundary layer*

The wall-layer streamfunction for $\eta = O(1)$ is governed by the fourth-order equation

$$\frac{\partial^4 \widetilde{\psi}}{\partial \eta^4} + 2\eta \frac{\partial^3 \widetilde{\psi}}{\partial \eta^3} = 0 \quad \text{for } 0 < \eta < \eta^*(\xi > \xi^*), \tag{3.11d}$$

subject to the homogeneous boundary conditions

$$\widetilde{\psi} = 0, \quad \widetilde{\psi}_\eta = 0 \quad \text{on } \eta = 0, \tag{3.13}$$

and matching with the core-flow solution obtained from (3.11*a*).

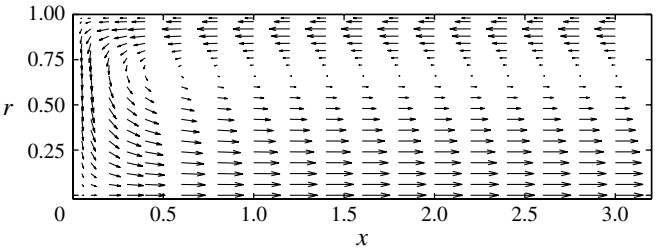

FIGURE 3. Plot of the velocity field within the pipe at time $T = 1.0 \times 10^{-3}$.

3.3.4. *The corner boundary layer*

The final region is the corner boundary layer, in which the modified streamfunction satisfies

$$\left(\frac{\partial^2}{\partial\eta^2}+\frac{\partial^2}{\partial\xi^2}\right)^2\widetilde{\psi}+2\eta\left(\frac{\partial^2}{\partial\eta^2}+\frac{\partial^2}{\partial\xi^2}\right)\frac{\partial\widetilde{\psi}}{\partial\eta}+2\xi\left(\frac{\partial^2}{\partial\eta^2}+\frac{\partial^2}{\partial\xi^2}\right)\frac{\partial\widetilde{\psi}}{\partial\xi}$$
$$=\left[\frac{\partial^4\psi_\infty}{\partial\eta^4}+2\eta\frac{\partial^3\psi_\infty}{\partial\eta^3}\right], \tag{3.11e}$$

subject to the following homogeneous and inhomogeneous boundary conditions:

$$\widetilde{\psi}=-\psi_\infty, \quad \widetilde{\psi}_\xi=0 \quad \text{on } \xi=0, \tag{3.11f}$$

$$\widetilde{\psi}=-\psi_\infty, \quad \widetilde{\psi}_\eta=0 \quad \text{on } \eta=0. \tag{3.11g}$$

3.4. *Boundary layer matching*

The end-region flow is fully specified by the system (3.11) of four partial differential equations. Each equation is linear and depends on the Reynolds number only implicitly, through the boundary-layer variables η and ξ. We first re-express the four boundary-layer equations in terms of the original coordinates (r, x) at some fixed time T taken here to be $T = T_0 = O(10^{-4})$. The equations are then solved simultaneously on a single grid of spectral collocation points in (r, x) space. The various matching conditions between the core-flow, the wall boundary layer and the blockage boundary layer are explicitly satisfied at the 'overlap' region defined by $\eta \approx \eta^*$ and $\xi \approx \xi^*$ (where η^* and ξ^* must be chosen suitably large to ensure convergence of the boundary layer solutions). After some considerable experimentation we found that the choice

$$\eta \approx \eta^* = 2.0 \quad \text{and/or} \quad \xi \approx \xi^* = 2 \tag{3.14}$$

delivered converged results. The spectral scheme and computational domain used for this purpose are identical to that described above and used for our full nonlinear calculations, importantly ensuring that the computed initial (small-time) flow state is fully compatible with the spatial discretization employed in the fully nonlinear problem. Note that the collocation points of this scheme are strongly clustered near the physical domain boundaries, to the extent that each boundary layer is resolved by $O(10)$ collocation points in the wall-normal coordinate. Notwithstanding the low analytical accuracy of (3.11), our numerical scheme proved robust both to the initialization time T_0 and to the boundary layer parameters η^* and ξ^*. A typical small-time solution is shown in figure 3.

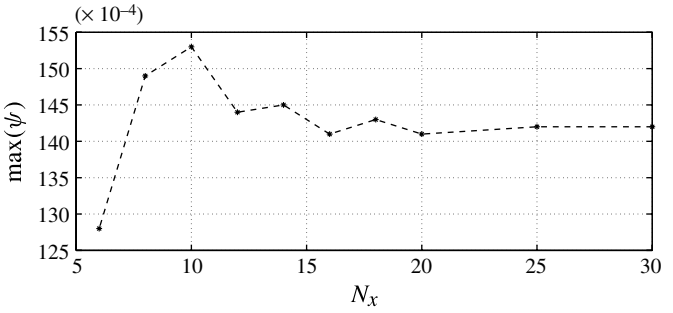

FIGURE 4. Plot of the maximum value of the streamfunction, at time $T = 0.05$, versus the number of scaled Laguerre functions used in our computations for a fixed Reynolds number $Re = 1000$ and $M = 22$ (M being the order of the pseudospectral discretization in the radial coordinate.

3.5. *Code validation and convergence*

We validated our code against a spin-up problem, namely the (regularized) lid-driven flow in an enclosed square cavity. The results from our Chebyshev-spectral test code are converged to six significant figures and compared well with those of Peyret & Taylor (1983). We also undertook extensive grid convergence tests to ensure that the results to be presented here are accurate. A typical result is shown in figure 4, where we present a plot of the maximum value of the streamfunction versus the number of scaled Laguerre functions N_x: convergence is rapid. A subsequent test of the radial decomposition demonstrates that fewer radial nodes are required to achieve high accuracy: for the Reynolds number $Re = 1000$ of figure 4, a value of M as small as 10 was able to reproduce the results to four significant figures. All the results presented here are for $N_x = 30$ and $N_r = 22$, and the results can be taken to have converged to within graphical accuracy.

4. Results and discussion

Turning now to a discussion of our results, we present, in figure 5, contours of the instantaneous streamfunction $\psi = \widetilde{\psi} + \psi_\infty$ in the decaying end-region flow for a relatively low pre-blockage Reynolds number of $Re = 500$ at various times. Since the pre-blockage flow is directed from left to right, the post-blockage flow comprises a rightward core-flow ($0 \leqslant r \lesssim 0.6$) balanced by a return flow down the blockage wall ($x = 0$) and a right-to-left reversed flow along the sidewall ($r = 1$). Since the flow is (highly) unsteady, the indicated contour-levels are not strictly guaranteed to coincide with physical streamlines; nevertheless, we have verified that the correspondence is very close. In an effort to track the decay process as closely as possible, figure 5 presents flow snapshots at $T = 0.001$ (i.e. almost immediately following the blockage event), $T = 0.005$, $T = 0.01$, and thereafter at intervals of $\Delta T = 0.01$ up to a maximum of $T = 0.10$. Although it is not immediately obvious from this figure, the overall flow field decays in magnitude relatively slowly during the first half of this period (characterized by expansion of the sidewall boundary layer to fill the pipe) and rapidly thereafter; indeed, at the end-point $T = 0.10$ the overall flow field has decayed by approximately one order of magnitude relative to its immediate post-blockage state. This behaviour is in full accord with that reported by Jewell & Denier (2006) for the flow $\psi_\infty(r, T)$ well upstream of the blockage. The most prominent feature of this

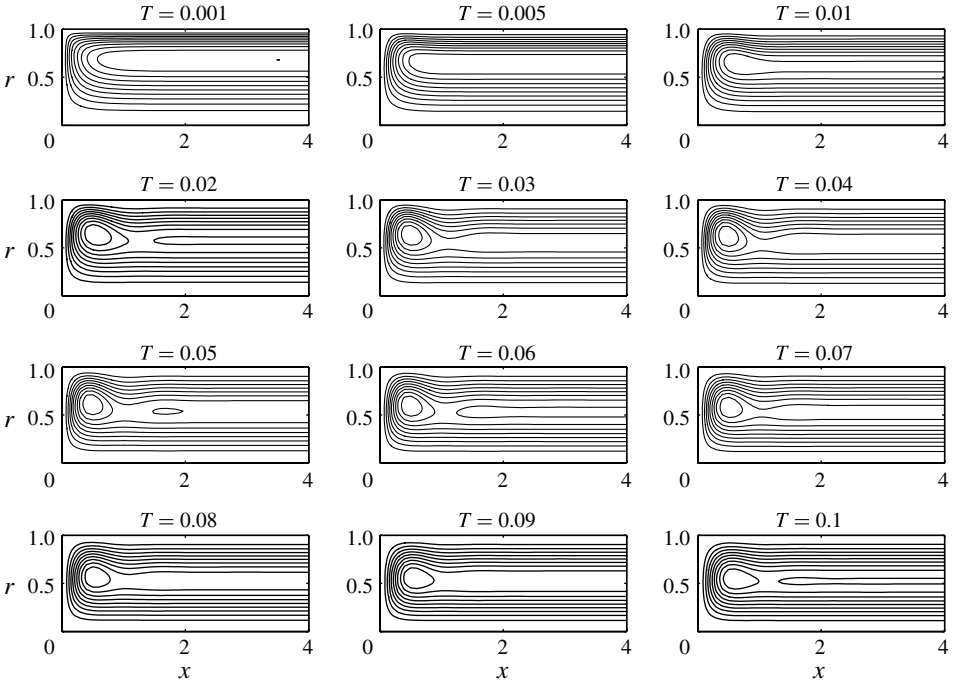

FIGURE 5. Contours of the streamfunction $\psi(r, x)$ for Reynolds number $Re = 500$ at times $T = 0.001, 0.005, \ldots, 0.10$ as indicated. Calculations were performed out to a streamwise distance of five pipe radii, although the flow domain is truncated here to $x_{max} = 4$ for display purposes. The flow is oriented leftward near the pipe wall ($u < 0$ for $0.6 \lesssim r < 1$), downward along the blockage wall ($v < 0$ for $0 < x \lesssim 0.5$), and rightward in the pipe interior ($u > 0$ for $0 \leqslant r \lesssim 0.6$). At the junction of these three domains, flow reversal results in a weak vortex for $T \gtrsim 0.01$.

end-region flow is the development of a *weak internal vortex* approximately one-third of a pipe diameter upstream of the blockage ($x \approx 0.7$) on the stagnation line ($r \approx 0.65$). Thus, the principal internal vortex is located near the junction between the four subregions of the end region identified in the Appendix, namely the core-flow, sidewall boundary layer, end-wall layer, and the corner boundary layer proper. This vortex is most prominent during the middle phase of the decay process ($0.02 \lesssim T \lesssim 0.07$), but shows no sign of subsiding completely. Moreover, a very weak secondary vortex appears briefly ($T \approx 0.05$) on the stagnation line at $x \approx 1.7$, whereas for $x \gtrsim 2$ all streamlines are essentially parallel. Thus, end-effects at $Re = 500$ are confined to a region approximately one diameter from the blockage.

We now consider the Reynolds number dependence of the decay process. Recall that the upstream laminar flow $\psi_\infty(r, T)$ is independent of the pre-blockage Reynolds number Re except through the rescaling $T = Re^{-1}t$ of the advective time t. The end-region decay process is illustrated in figures 6–8 for $Re = 1000$, $Re = 2000$ and $Re = 3000$ respectively. As in figure 5 for the case $Re = 500$, we plot pseudo-streamlines of the flow at time intervals of $\Delta T = 0.01$. With increasing Reynolds number the primary internal vortex develops more rapidly, becomes substantially more vigorous, and is more constricted in a geometric sense. It is unmistakable for $T \geqslant 0.02$ at $Re = 500$, for $T \geqslant 0.01$ at $Re = 1000$ (figure 6), and for $T \geqslant 0.005$

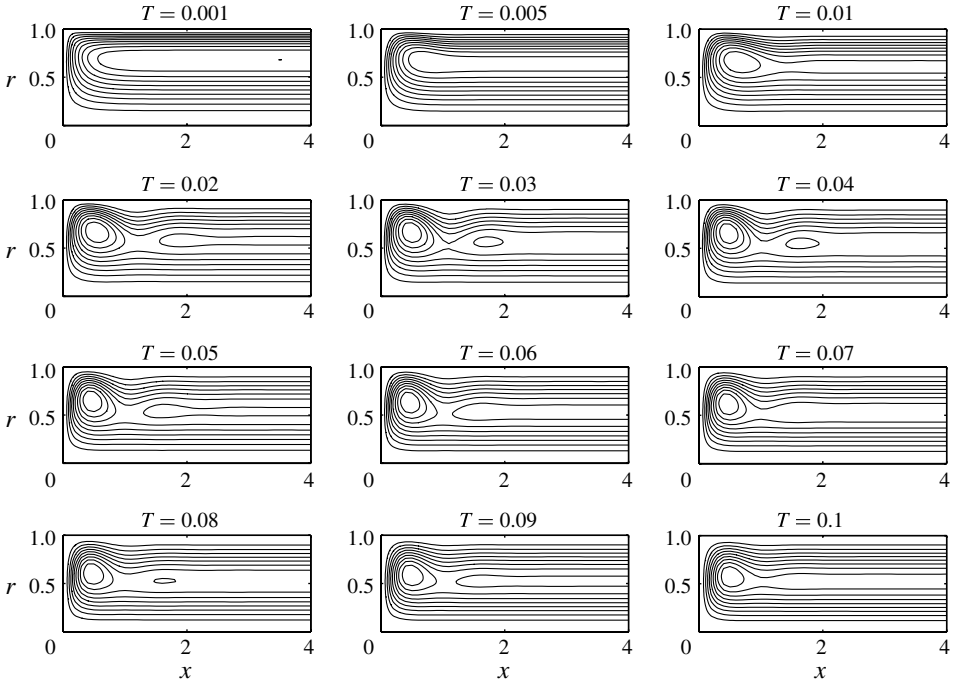

FIGURE 6. Contours of the streamfunction $\psi(r, x)$ for Reynolds number $Re = 1000$.

at $Re = 2000$ (figure 7); nonetheless, its temporal evolution is qualitatively similar throughout. Likewise, the secondary internal vortex is well developed by $T = 0.05$, $T = 0.03$ and $T = 0.02$ at $Re = 500$, $Re = 1000$ and $Re = 2000$ respectively. A tertiary stagnation-line vortex ($x \approx 3.0$) appears embryonically at $Re = 2000$ and is well developed at $Re = 3000$ (figure 8) for $0.03 \lesssim T \lesssim 0.05$. Thus, the streamwise extent of the end region increases significantly as a function of Reynolds number, from approximately one diameter at $Re = 500$ to two diameters at $Re = 3000$.

Though useful for identifying internal vortices, the streamfunction plots of figures 5–8 have some inherent deficiencies. In particular, they gloss over the boundary layers and give no clear indication of the velocity magnitude on and near the centreline $r = 0$. Both weaknesses reflect the mathematical property that $\psi \to 0$ quadratically in each of the limits $r \to 1$, $x \to 0$ and $r \to 0$. To complement the streamline plots, therefore, we present quiver-plots and (u, v) contour-plots of the flows for $Re = 500$ (figure 9), $Re = 1000$ (figure 10) and $Re = 2000$ (figure 11). To conserve space, only five snapshots are presented for each flow (versus twelve in figures 5–8) out to a streamwise distance of $x = 2$. Throughout, the stagnation line $u = 0$ is highlighted and the velocity arrows are scaled lengthwise with respect to velocity magnitude; the absolute velocities, meanwhile, may be gauged via the indicated contour spacings Δu and Δv. For example, in figure 10 for $Re = 1000$ the absolute velocity range varies from $\{-0.344 < u < 0.463, -0.269 < v < 0.001\}$ in the initial snapshot ($T = 0.001$) to $\{-0.028 < u < 0.077, -0.040 < v < 0.009\}$ in the final snapshot ($T = 0.08$). The composite diagrams of figures 9–11 clearly illustrate the boundary layers, the primary internal vortex, and a small corner vortex at $(x, r) = (0, 1)$. The mid-phase flow at $Re = 2000$ (figure 11) also exhibits a prominent

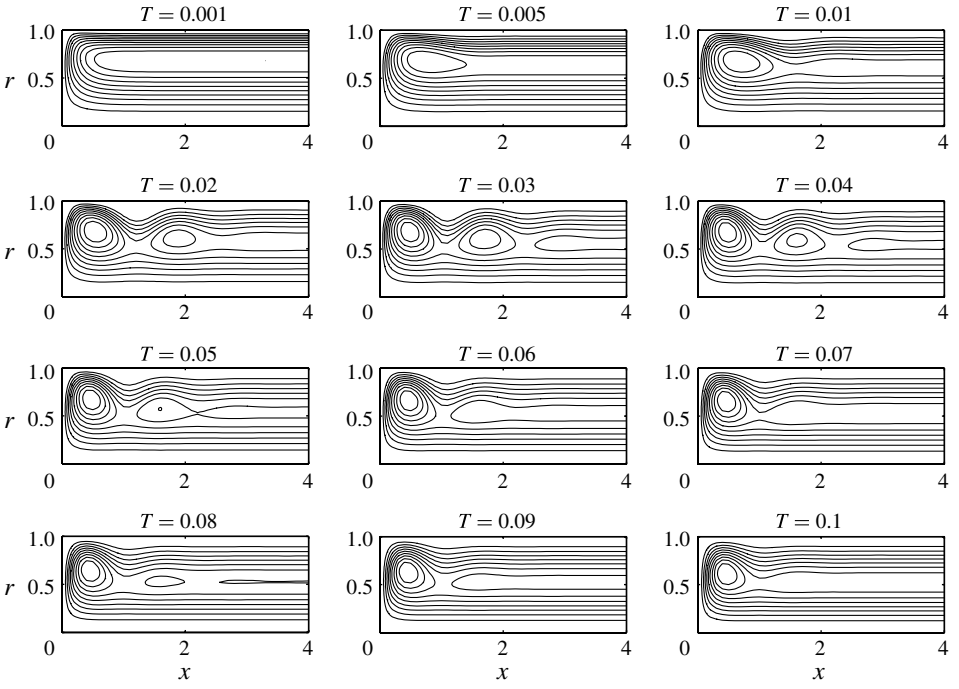

FIGURE 7. Contours of the streamfunction $\psi(r, x)$ for Reynolds number $Re = 2000$.

secondary internal vortex and, midway between these two vortices ($x \approx 1.1$), a weak recirculation bubble of forward flow on the sidewall $r = 1$. All non-trivial flow features in figures 9–11 are most vigorous during the mid-phase of decay, as suggested by the streamline plots. The streamfunction plots of wall and corner vortices register as blank spots in figures 5–8, albeit noticeably deflecting the neighbouring streamlines. We return to this point shortly.

Figures 9–11 also highlight the dynamics of forward and reverse flow, which by definition have equal flux. In the large-x upstream limit, the core region contracts significantly in size over the decay cycle, occupying 50 % of the pipe cross-section at $T = 0^+$ ($0 \leqslant r < 0.707$) but only 27 % at $T = 0.10$. This shrinkage is offset by a rapid weakening of the outer-region reversed flow relative to the forward flow, from 1:1 at $T = 0^+$ ($-1/2 \leqslant u \leqslant +1/2$) to approximately 4:1 at $T = 0.10$ ($-0.012 < u < 0.047$). The stagnation-line vortices, however, induce an outward radial bulging of the core region, which serves to change the respective size of the regions of forward and reversed flow. The competing trends of core contraction and bulging of the end region, due to the stagnation-line vortices, are readily discernible in figure 11. Unsurprisingly, the rebalancing effect increases as a function of Reynolds number. At $T = 0.02$, for example, the ratio of maximum forward to reverse flow changes from 2.66:1 at $Re = 100$ to 1.93 at $Re = 500$, 1.54 at $Re = 1000$, 1.41 at $Re = 1500$, and 1.33 at $Re = 2000$.

Returning to the wall and corner vortices identified in figure 11, we present in figure 12 an enhanced contour plot of the streamfunction over times from $T = 0.015$ to $T = 0.06$ at pre-blockage flow Reynolds number of $Re = 3000$. From this figure we can clearly observe the expansion of the tertiary wall vortex at small times and

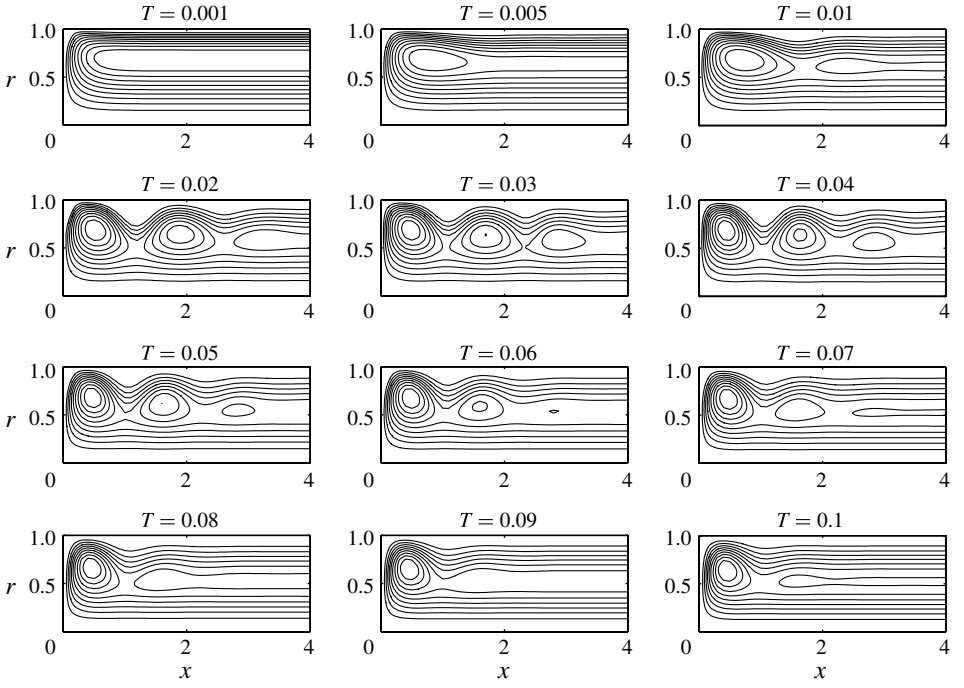

FIGURE 8. Contours of the streamfunction $\psi(r, x)$ for Reynolds number $Re = 3000$.

the presence of a small corner vortex. This wall vortex grows, and in doing so distorts the flow within the corner, thus generating the smaller-scale corner vortex. This corner vortex grows as the larger wall vortex decays. This wall vortex now grows, again distorting the corner streamlines until the corner vortex disappears. At time $T = 0.04$ (figure 12*f*) the wall vortex begins to decay again, allowing the growth of a smaller vortex in the corner which persists within the corner boundary layer at $(r, x) = (1, 0)$. The overall behaviour of the smaller wall vortices is largely controlled by the dynamics of the decaying primary and secondary vortices within the body of the flow.

This primary wall vortex is also discernible in the cross-sectional plots of the axial velocity presented in figure 13, manifesting as a thin outer ring of forward flow ($u > 0$, heavy shading) for $T = 0.02$ and $T = 0.05$ at the streamwise station $x = 1$. The observed generation of small toroidal wall vortices is reminiscent of the behaviour of the flow in a driven cylinder considered by Mullin *et al.* (2000). In that problem (see also Jahnke & Valentine 1996), the creation of the stagnation points can be attributed to the generation of an adverse pressure gradient due to the differential rotation on the cylinder, which in turn induces separation of the boundary layer on the surface of the cylinder. In the current problem the adverse pressure gradient which drives the boundary layer separation, giving rise to the wall vortex, arises as a result of the change of the unsteady (decaying) core-flow. Some preliminary experimental validation of these results, and clear evidence for the wall vortices, can be found in Toophanpour-Rami *et al.* (2007). Qualitatively similar vortices were also observed by Das & Arakeri (1998), who considered the unsteady flow generated by a piston in a pipe (as a model of the suddenly blocked flow considered here).

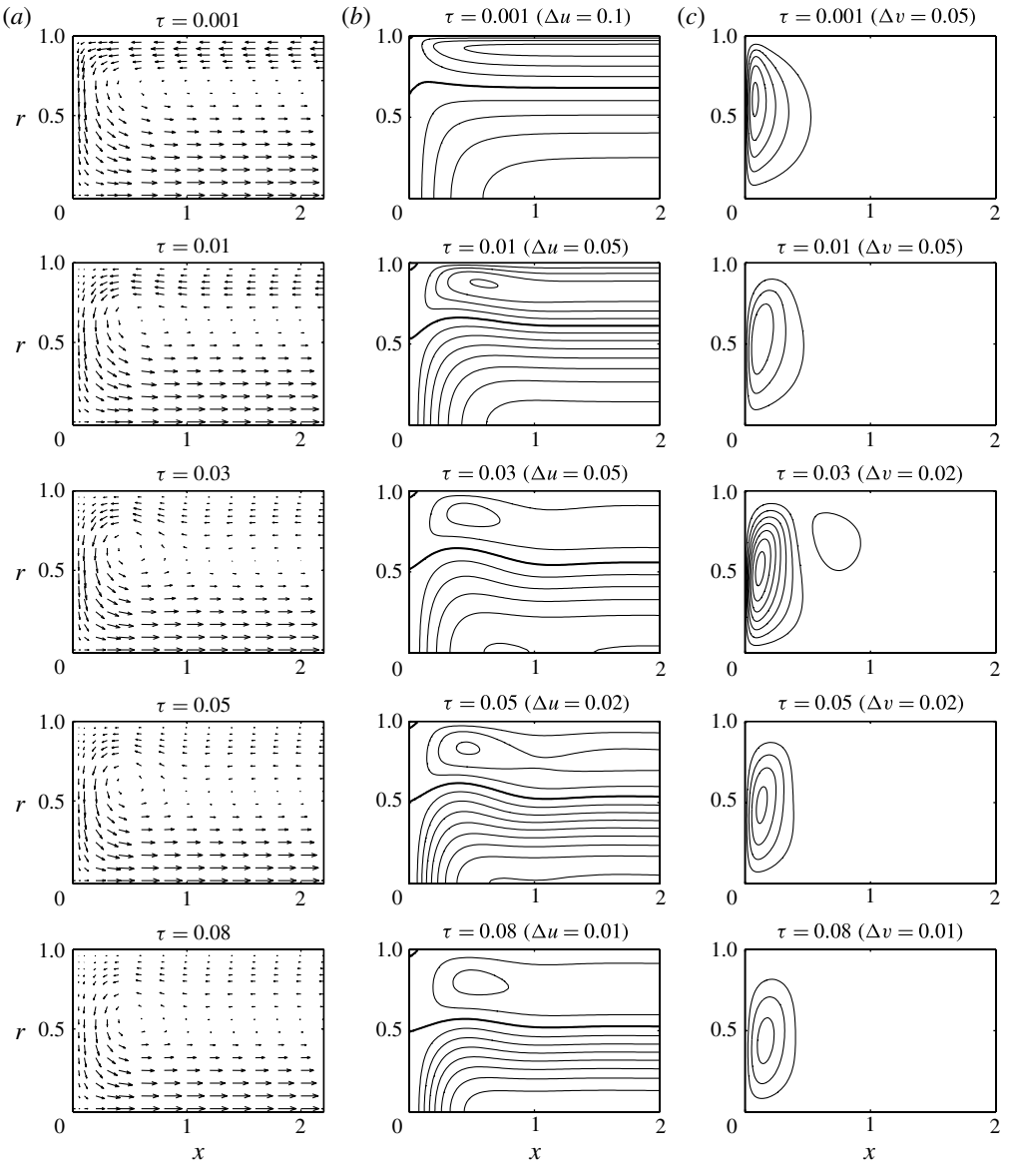

FIGURE 9. (*a*) Quiver plots of the flow at $Re = 500$, shown for $x \leqslant 2$ at times $T = 0.001$, 0.01, 0.03, 0.05 and 0.08. (*b*) Contours of streamwise velocity u, with contour spacing Δu as indicated; the heavy contour corresponds to the stagnation line $u = 0$. (*c*) Contours of radial velocity v, with spacing Δv as indicated (zero contour not shown).

The generation of the primary vortex (and subsequent generation of second, and tertiary, vortices) occurs as a result of the formation of the corner boundary layer. This boundary layer develops in order to allow the initially inviscid flow to adjust to the full no-slip conditions on the pipe wall and at the blockage. Its presence in the flow serves to decelerate the flow within the wall boundary layer (the axial pressure gradient becoming adverse as a result of the blocking effect of this corner boundary layer). When the axial pressure gradient becomes sufficiently adverse it forces the

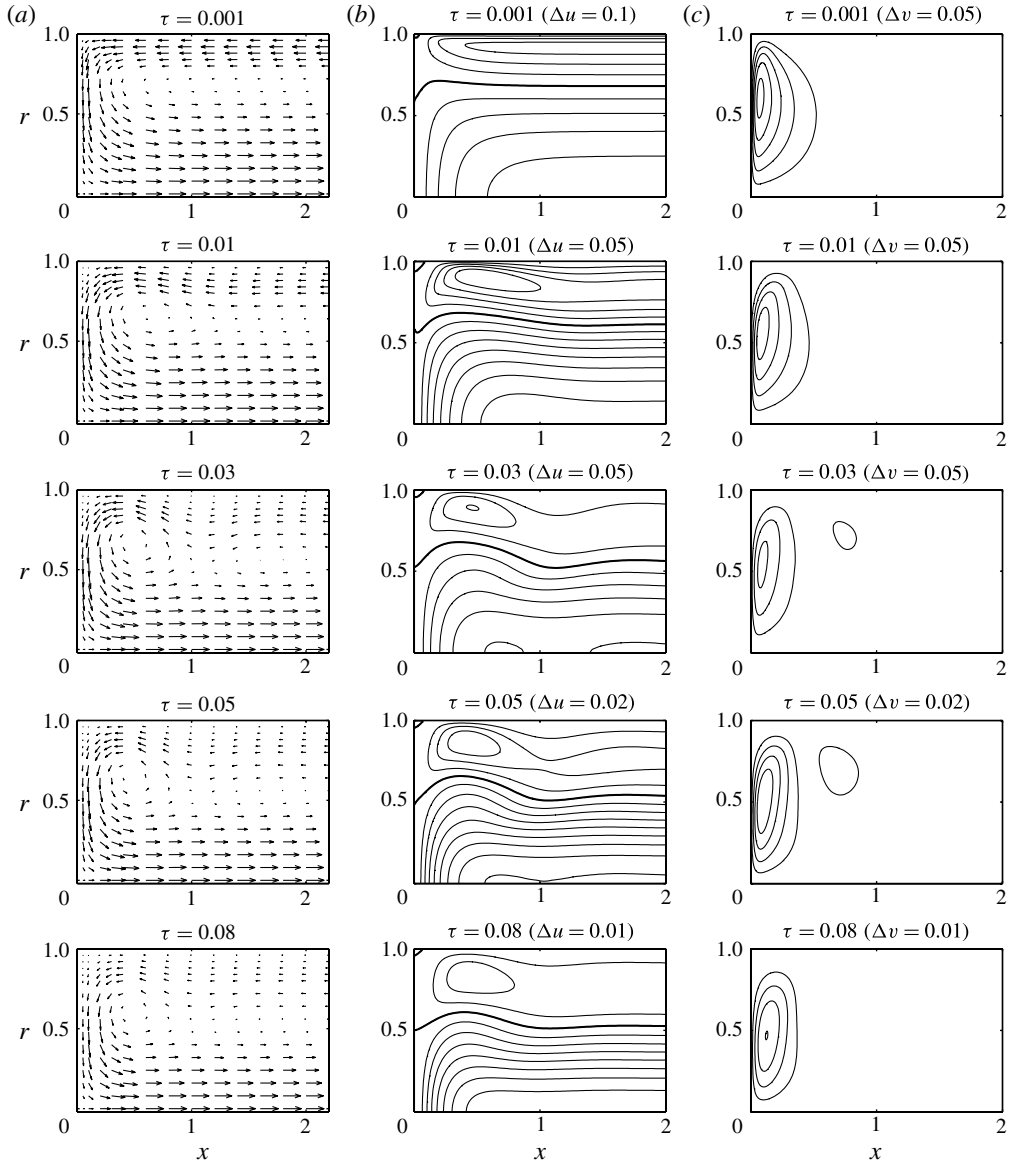

FIGURE 10. Quiver and contour plots of the flow at $Re = 1000$, shown for $x \leqslant 2$ at times $T = 0.001$, 0.01, 0.03, 0.05 and 0.08 as indicated.

boundary layer on the pipe wall to detach, resulting in the small wall vortex (the attached recirculation region seen most clearly in the $Re = 3000$ results presented in figure 12). The time and location at which this boundary-layer separation occurs depends strongly upon the Reynolds number, with the onset time decreasing and the position of separation moving closer towards the blockage region with increasing Re.

The first separation of the pipe-wall boundary layer serves to deflect the adjacent streamlines (figures 5–8). The stagnation line seen in the small-time solution (figure 2) is then deflected within the vicinity of the axial location of the separation point,

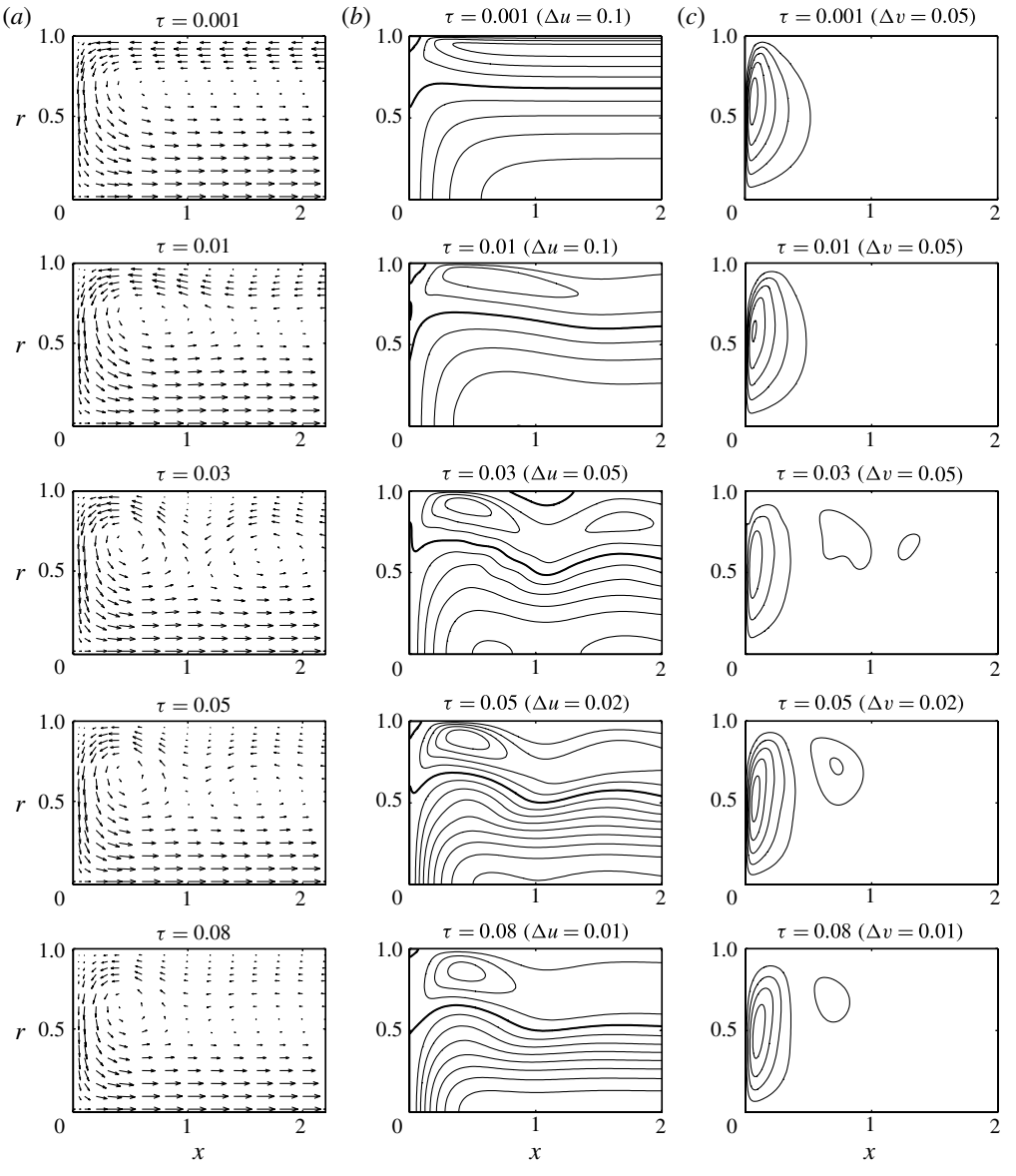

FIGURE 11. Quiver and contour plots of the flow at $Re = 2000$, shown for $x \leqslant 2$ at times $T = 0.001$, 0.01, 0.03, 0.05 and 0.08 as indicated.

thus serving to generate the first primary vortex in the end region. This process of boundary-layer separation continues, generating the further vortices observed within the end region.

The intensity of vortices in the end region, and their impact upon the flows decay time, is illustrated in figure 14 where we plot the global absolute maximum magnitude of the streamfunction as a function of T and Re. Geometrically, this maximum is attained in the upstream limit $x \to \infty$ for moderate Re or small T. In this region the flow intensity exhibits a rapid (exponential) decay; observe the rapid exponential-like

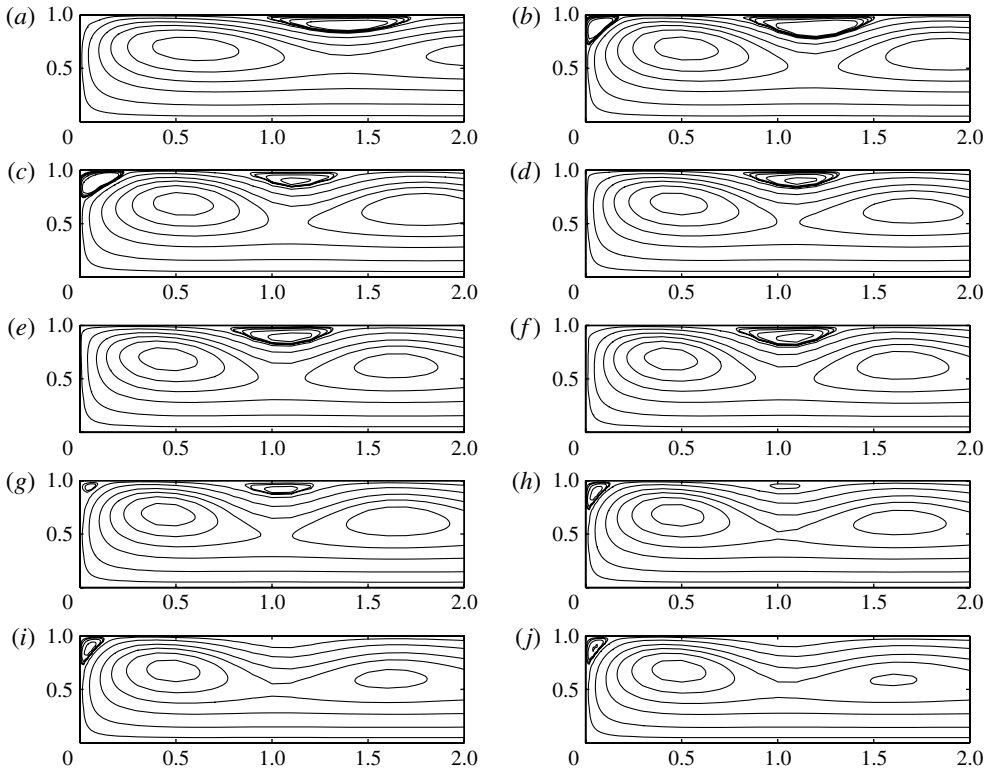

FIGURE 12. Contour plots of the streamfunction $\psi(r, x)$ for Reynolds number $Re = 3000$, shown for $x \leqslant 2$ and $0.015 \leqslant T \leqslant 0.60$ in steps of $\Delta T = 0.05$ (figures *a–j* respectively). The corner vortex and principal wall vortex are highlighted by heavy contours at $\psi = -0.0125$ and $\psi = 0.00125 \times 2^i$ ($i = 1, \ldots, 4$). The equispaced light contours correspond to $\psi = -0.9$ to -0.1 (in steps of 0.2).

decay for the case $Re = 250$ compared to the slower decay for higher Re. This change is manifest in figure 14, with the small Re flows exhibiting an exponential-like decay governed by the linear dynamics of the downstream flow. For higher Re the flow decay is governed by the dynamics of the near-blockage region, the maximum now coinciding with the centre of the primary internal vortex, which can clearly be identified in figures 3–8.

5. Conclusions

We have considered the behaviour of the flow that arises when classical Hagen–Poiseuille flow in a pipe is inhibited by the imposition of a sudden complete blockage. Our primary concern has been to elucidate the behaviour of the flow in the vicinity of the blockage, thus allowing us to build upon the early work of Weinbaum & Parker (1975) and provide a complete description of the laminar decay of the flow. Under the assumption of axisymmetric flow we have demonstrated that the post-blockage flow develops a series of vortices which impact significantly upon the decay time of the flow. Our results uncover a complicated process of vorticity generation and unsteady boundary-layer separation at the pipe walls.

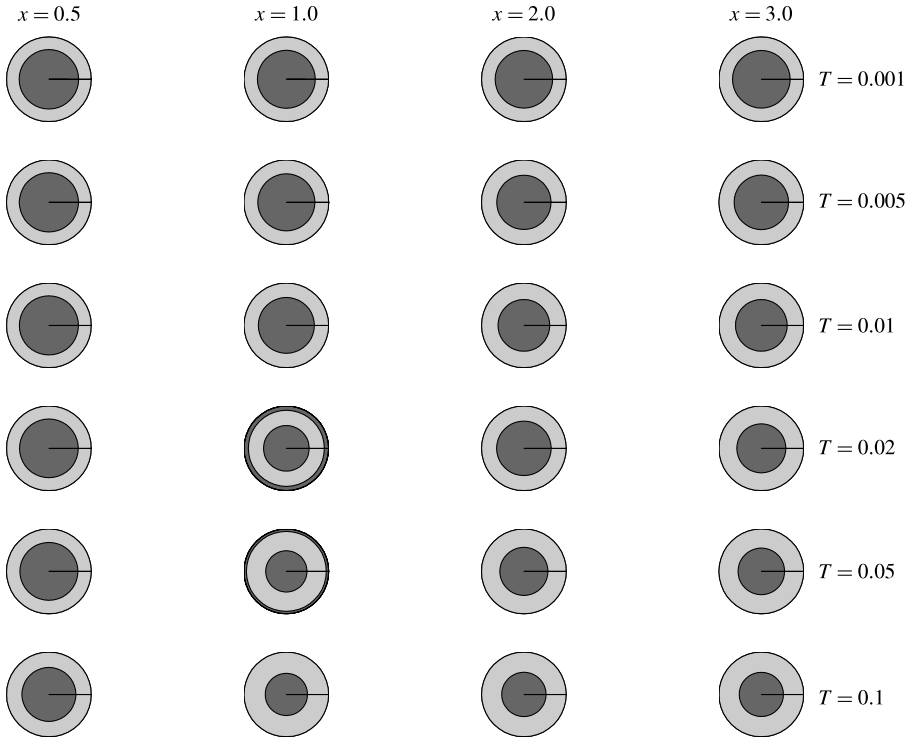

FIGURE 13. Cross-sectional contour plots of axial velocity for $Re = 3000$ at selected times and streamwise stations. The dark shaded region corresponds to forward flow ($u > 0$) and the light shaded region corresponds to reversed flow ($u < 0$). For $T = 0.02$ and $T = 0.05$, the thin outer ring of forward flow at $x = 1$ corresponds to the principal wall vortex highlighted in the previous figure.

The physical mechanism leading to the generation of these end-region vortices can be attributed to the behaviour of the boundary layers that develop after the imposition of the blockage. The sudden blockage of the pipe results in the development of viscous boundary layers at both the pipe wall and the blockage connected via a corner boundary layer structure. The development of this corner boundary layer acts to decelerate the streamwise flow near the pipe-wall–blockage junction (as the flow must necessarily slow in order to negotiate the corner region). This deceleration of the flow then renders the unsteady axial pressure gradient, which controls the development of the unsteady wall boundary layer, adverse when compared to the wall boundary layer far upstream of the blockage. This blockage effect on the, now, adverse pressure gradient becomes sufficient large (at some particular time and axial location, both of which are dependent upon the Reynolds number) to allow the unsteady boundary layer to separate. The separation serves to deflect the flow streamlines, with the consequence that the streamline closes near the blockage and consequently a vortex forms in that region. This process continues as the flow decays, resulting in further boundary layer separations and subsequent vortex generation in the 'core' region of the flow, the strength of these vortices increasing with increasing Reynolds number.

Having described the full details of the laminar post-blockage flow, it is now feasible to consider the related question of the behaviour of the flow when the

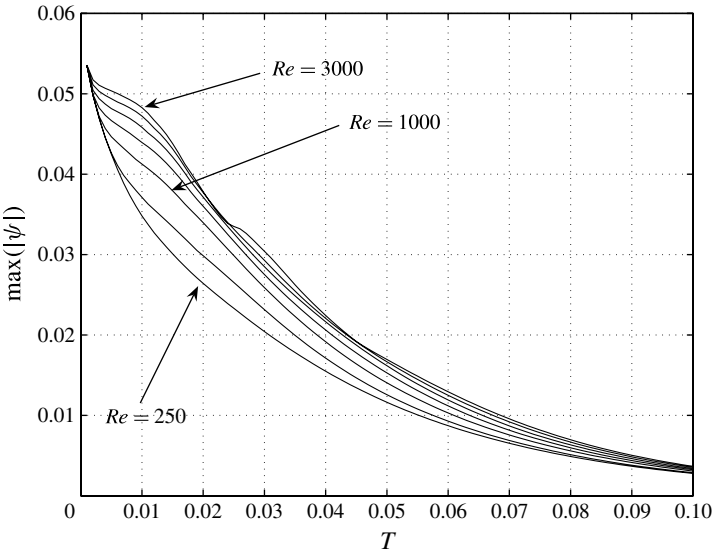

FIGURE 14. Global maximum of $|\psi(r, x)|$, plotted as a function of T for Reynolds numbers of $Re = 250$, 500, 1000, 1500, 2000, 2500 and 3000.

blockage is removed (or further, when a blockage is applied periodically, as occurs in the aortic valve and the pulmonic valve during ventricular ejection). Of course, our constraint of axisymmetric flow precludes the development of instabilities in the region away from the blockage (as it is only non-axisymmetric disturbances that grow there) and thus any subsequent analysis would necessarily be restricted to the dynamics of the laminar flow. Putting aside the question of flow stability for the moment, we can make some tentative comments on the possible flow after removal of the blockage. Just as with the sudden imposition of the blockage, the sudden removal of the blockage will result in an instantaneous flow in which the vorticity is frozen in its blocked state. This vorticity, consisting of the vortices generated during the blocked phase (on both sides of the blockage), will now be advected downstream. It is not clear whether these vortices would decay or persist but we would expect them to play an important (but as yet undetermined) role in the subsequent flow dynamics.

Of course, the question still remains as to how (and indeed where) the flow first becomes unstable and undergoes a transition to a turbulent state and at what Reynolds number this first occurs. We cannot answer this question fully here but it is useful to make some general comments. Upon reviewing the results of Jewell & Denier (2006) we find that a linear (quasi-steady) analysis of the unidirectional upstream flow $\psi_\infty(r, T)$ shows the flow to be stable to axisymmetric disturbances and weakly unstable to non-axisymmetric disturbances during the mid-decay phase for Reynolds numbers as low as $Re = 500$. Upon relaxing the quasi-steady assumption, however, Jewell & Denier (2006) postulated a lower limit of $Re_c \approx 1000$ for complete breakdown of the laminar structure. This latter figure is still well below the experimental result of $Re_c \approx 2000$ reported by Weinbaum & Parker (1975), but in good qualitative agreement with the findings of Das & Arakeri (1998) for impulsive flow in a small piston. Moreover, the 'asymmetric' nature of breakdown reported by Das & Arakeri (1998) is consistent with the predicted instability mode of azimuthal wavenumber $k = 1$. One could conjecture that the axisymmetric flow postulated in the

present work is unlikely to persist much above $Re = 1000$ and furthermore, given the presence of the vortex structure(s) within the end region, that this region may well provide the dominant contribution to the full transition in this flow. We hope to present an answer to this question in a future paper.

Acknowledgements

N.J. gratefully acknowledges the support of an Australian Postgraduate Award and J.P.D. the support of the Australian Research Council through grant DP0556360. We are grateful for the insightful comments of the three referees, comments that served to improve the presentation of this paper.

Appendix. The small-time structure of the flow

In order to develop a small-T asymptotic solution for the flow in the vicinity of the blockage we allow ourselves to be led by the analysis of Jewell & Denier (2006), who demonstrated that, for $x \gg 1$ and $0 < T \ll 1$, the flow develops a boundary layer of thickness $O(\sqrt{T})$ on the pipe wall. This boundary layer structure will persist into the end region $x = O(1)$ before breaking down in the immediate vicinity, i.e. within an $x = O(\sqrt{T})$ distance from the end-wall (at which point there is a balance between streamwise and radial diffusion). A similar argument indicates the existence of a boundary layer of thickness $O(\sqrt{T})$ for $1 - r = O(1)$ on the blockage wall $x = 0$, wherein the radial velocity v adjusts to the no-slip condition before breaking down at $1 - r = O(\sqrt{T})$. The sidewall and end-wall boundary layers will intersect for $x = O(\sqrt{T})$ and $1 - r = O(\sqrt{T})$ in a locally square corner boundary layer. Binding these three regions together will be an inviscid core-flow for $x = O(1)$ and $1 - r = O(1)$.

These four subregions of the blockage region are shown schematically in figure 15. In this figure – and throughout the remainder of this paper – we orient the pre-blockage flow from left to right, so that the streamwise coordinate x is positive throughout the region of interest. In other words, the end region is defined by $0 \leqslant x \leqslant O(1)$; the pre-blockage Poiseuille flow is given by $u(r, t < 0) = 1 - r^2$; and the post-blockage upstream flow for $x \gg 1$ comprises a right-directed core-flow ($u > 0$) balanced by a left-directed return flow ($u < 0$) along the sidewall $r = 1$.

To obtain a small-T starting solution, we must develop a solution to the governing equations in each of the four regions illustrated in figure 15. We consider each region in turn.

A.1. *The wall boundary layer in which* $r \approx 1$

The wall boundary layer is defined by $1 - r = O(\sqrt{T})$ with $x = O(1)$. Within this layer the axial velocity u adjusts to the no-slip boundary conditions on the pipe wall. To determine the flow herein, we first note that $u = O(1)$ and $v = O(\sqrt{T})$, while their respective wall-normal gradients are $O(T^{-1/2})$ and $O(1)$. Thus, the axial momentum equation possesses viscous and advective terms of orders $O(T^{-1})$ and $O(Re)$, compared with $O(T^{-1/2})$ and $O(Re\sqrt{T})$ respectively for the radial momentum equation. It follows that for $T \ll Re^{-1}$ the flow is effectively driven by viscosity (and consequently weakly nonlinear), whereas for $T > Re^{-1}$ it is advective and strongly nonlinear. This observation allows us to make some progress in obtaining the small-T solution for the full Navier–Stokes equations.

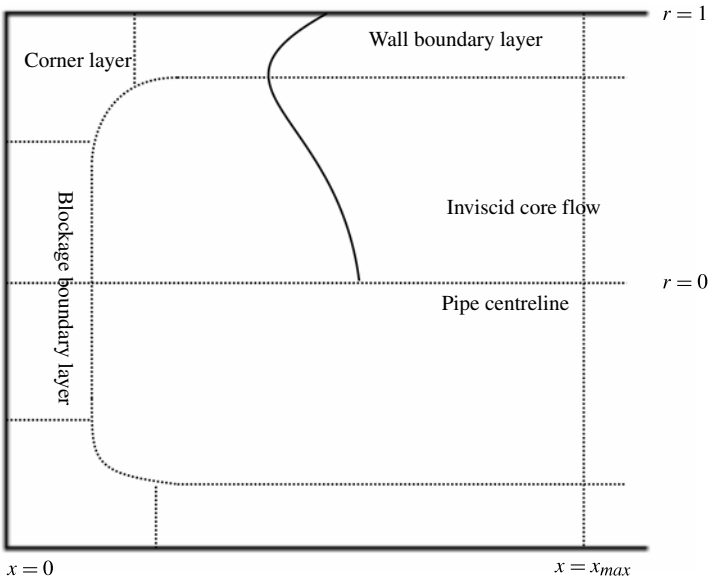

FIGURE 15. Schematic of the small-time asymptotic structure of the near-blockage flow.

Following Jewell & Denier (2006), we begin by defining the boundary layer coordinate η via

$$1 - r = 2\sqrt{T}\eta, \tag{A 1}$$

where the factor of 2 is included purely for analytic convenience. In the region defined by $\eta = O(1)$, the flow can be written as

$$u(r, x, t) = R_u(\eta)X_u(x) + O(\sqrt{T}, TRe), \tag{A 2a}$$

$$v(r, x, t) = R_v(\eta)X_v(x) + O(T, T^{3/2}Re). \tag{A 2b}$$

Substituting the u-expression (A 2a) into the Navier–Stokes equations and retaining leading-order terms, we obtain the following ordinary differential equation for the η-dependent component of the solution

$$\frac{\mathrm{d}^2 R_u}{\mathrm{d}\eta^2} + 2\eta\frac{\mathrm{d}R_u}{\mathrm{d}\eta} = 0. \tag{A 3}$$

Solving this subject to the boundary conditions $R_u(0) = 0$ and $R_u(\eta) \to 1$ as $\eta \to \infty$ yields the familiar error-function boundary layer profile

$$R_u(\eta) = \mathrm{erf}(\eta). \tag{A 4}$$

The x-dependence of the axial velocity is then found by matching with the core-flow in the limit $\eta \to \infty$. To leading order, this is the velocity $u_0(r = 1, x)$ at time $T = 0^+$ from (2.2) and (2.3):

$$X_u(x) = -\frac{1}{2} - 4\sum_{k=1}^{\infty} \lambda_k^{-2}\left[\frac{\mathrm{J}_0(\lambda_k)}{\mathrm{J}_2(\lambda_k)}\right]\exp(-\lambda_k x), \quad (x > 0). \tag{A 5}$$

We can now determine the leading-order component of the radial velocity by integrating the continuity equation with respect to x, to yield

$$R_v(\eta) = \int_0^\eta \mathrm{erf}(s)\,\mathrm{d}s \quad \text{and} \quad X_v(x) = -2\sqrt{T}\left[\frac{\partial v_0}{\partial r}(r=1,x)\right]. \tag{A 6}$$

A.2. *The blockage boundary layer for which* $0 < x \ll 1$

The wall boundary layer is defined by $x = O(\sqrt{T})$ with $1 - r = O(1)$ and $\eta \gg 1$. Within this layer the radial velocity v along the end-wall $x = 0$ adjusts to the no-slip condition. The analysis of the flow in this region follows that given above for the wall boundary layer with the roles of u and v reversed. In particular, we find that $v = O(1)$ and $u = O(\sqrt{T})$, with the viscous and advective terms dominating for $T \ll Re^{-1}$ and $T > Re^{-1}$ respectively. We define a new axial boundary layer variable ξ by

$$x = 2\sqrt{T}\xi, \tag{A 7}$$

analogous with the definition of η in (A 1). For $0 < T \ll Re^{-1}$ and $\xi = O(1)$, we find that

$$u = 2\sqrt{T}\left[\frac{\partial u_0}{\partial x}(r,0)\right]\int_0^\xi \mathrm{erf}(s)\,\mathrm{d}s + O(T, T^{3/2}Re), \tag{A 8a}$$

$$v = v_0(r,0)\mathrm{erf}(\xi) + O(\sqrt{T}, TRe). \tag{A 8b}$$

A.3. *The corner region for which* $r \approx 1$ *and* $0 < x \ll 1$

The corner boundary layer region is defined by $\eta = O(1)$ and $\xi = O(1)$, i.e. $x = O(\sqrt{T})$ with $1 - r = O(\sqrt{T})$. In this region u and v adjust to the no-slip boundary condition on $\eta = 0$ and $\xi = 0$ respectively. Consideration of the limit $x \to 0$ in (A 2) and (A 6) (or alternatively, the limit $r \to 1$ in (A 8)) shows that both u and v are $O(\sqrt{T})$ within the corner region. Thus we seek a solution of the form

$$(u, v) = \sqrt{T}(U(\eta,\xi), V(\eta,\xi)) + O(T, TRe). \tag{A 9}$$

Substitution into the full Navier–Stokes equations yields, at leading order (assuming that $ReT \ll 1$),

$$2\left(U - \eta\frac{\partial U}{\partial \eta} - \xi\frac{\partial U}{\partial \xi}\right) = \frac{\partial P}{\partial \xi} + \frac{\partial^2 U}{\partial \eta^2} + \frac{\partial^2 U}{\partial \xi^2}, \tag{A 10a}$$

$$2\left(V - \eta\frac{\partial V}{\partial \eta} - \xi\frac{\partial V}{\partial \xi}\right) = \frac{\partial P}{\partial \eta} + \frac{\partial^2 V}{\partial \eta^2} + \frac{\partial^2 V}{\partial \xi^2}, \tag{A 10b}$$

together with the equation of continuity

$$\frac{\partial U}{\partial \xi} + \frac{\partial V}{\partial \eta} = 0. \tag{A 11}$$

Introducing a streamfunction ψ in the usual way, we may eliminate U, V and P from (A 10) to give

$$\left(\frac{\partial^2}{\partial \eta^2} + \frac{\partial^2}{\partial \xi^2}\right)^2 \psi + 2\eta\left(\frac{\partial^2}{\partial \eta^2} + \frac{\partial^2}{\partial \xi^2}\right)\frac{\partial \psi}{\partial \eta} + 2\xi\left(\frac{\partial^2}{\partial \eta^2} + \frac{\partial^2}{\partial \xi^2}\right)\frac{\partial \psi}{\partial \xi} = 0. \tag{A 12}$$

This equation must be solved subject to no-slip boundary conditions on the pipe wall ($\eta = 0$) and at the blockage ($\xi = 0$), together with conditions ensuring matching with

the pipe-wall boundary layer, the blockage boundary layer solution and the inviscid core-flow solution.

REFERENCES

ABRAMOWITZ, M. & STEGUN, I. A. 1965 *Handbook of Mathematical Functions*. Dover.

BRUNONE, B., GOLIA, U. M. & GRECO, M. 1991 Some remarks on the momentum equations for fast transients. In *Hydraul. Transients in Column Separation, IAHR, Valencia, Spain*, pp. 201–209.

CLARKE, R. & DENIER, J. P. 2009 The decay of suddenly-blocked flow in a curved pipe. *J. Engng Maths* **63**, 241–257.

DAS, D. & ARAKERI, J. H. 1998 Transition of unsteady velocity profiles with reverse flow. *J. Fluid Mech.* **374**, 251–283.

FORNBERG, B. 1996 *A practical guide to pseudospectral methods*. Cambridge Monographs on Applied and Computational Mathematics, Cambridge University Press.

GHIDAOUI, M. S. & KOLYSHKIN, A. A. 2001 Stability analysis of velocity profiles in water-hammer flows. *J. Hydraul. Engng* **127**, 499–512.

GHIDAOUI, M. S. & KOLYSHKIN, A. A. 2002 A quasi-steady approach to the instability of time-dependent flows in pipes. *J. Fluid Mech.* **465**, 301–330.

GHIDAOUI, M. S. & MANSOUR, S. 2002 Efficient treatment of the Vardy–Brown unsteady shear in pipe transients. *J. Hydraul. Engng* **128**, 102–112.

HALL, P. & PARKER, K. H. 1976 The stability of the decaying flow in a suddenly blocked channel. *J. Fluid Mech.* **75**, 305–314.

JEWELL, N. 2009 The development and and stability of some non-planar boundary-layer flows. PhD thesis, University of Adelaide, Australia.

JEWELL, N. D. & DENIER, J. P. 2006 The instability of the flow in a suddenly blocked pipe. *Q. J. Mech. Appl. Maths* **59**, 651–673.

JAHNKE, C. C. & VALENTINE, D. T. 1996 Boundary-layer separation in a rotating cylinder. *Phys. Fluids* **8** (6), 1408–1414.

LAMBERT, M. F., VITKOSKY, J. P., SIMPSON, A. R. & BERGANT, A. 2001 A boundary-layer growth model for one-dimensional turbulent unsteady pipe friction. In *Proceedings of Australasian Fluid Mechanics Conference, Adelaide* (ed. B. Dally), pp. 929–932.

LIGGETT, J. A. & CHEN, L.-C. 1994 Inverse transient analysis in pipe networks. *J. Hydraul. Engng* **120**, 934–955.

MADDEN, F. N. & MULLIN, T. 1994 The spin-up from rest of a fluid-filled torus. *J. Fluid Mech.* **265**, 217–244.

MULLIN, T., KOBINE, J. J., TAVENER, S. J. & CLIFFE, K. A. 2000 On the creation of stagnation points near straight and sloped walls. *Phys. Fluids* **12**, 425–431.

NEREM, R. M. & SEED, W. A. 1972 An *in vivo* study of aortic flow disturbances. *Cardio. Res.* **6**, 1–14.

NISHIHARA, K., KNISLEY, C. W., NAKAHATA, Y., WADA, I. & IGUCHI, M. 2009 Transition to turbulence in constant velocity pipe flow after initial constant-acceleration. *J. Japan Soc. Exp. Mech.* **9**, 30–35.

NISHIHARA, K., NAKAHATA, Y., UEDA, Y., KNISLEY, C. W., SASAKI, Y. & IGUCHI, M. 2010 Effect of initial acceleration history on transition to turbulence in pipe flow. *J. Japan Soc. Exp. Mech.* **10**, 20–25.

PEYRET, R. & TAYLOR, T. D. 1983 *Computational Methods for Fluid Flow*. Springer Series in Computational Physics, Springer.

TOOPHANPOUR-RAMI, M., HASSAN, E. R., KELSO, R. M. & DENIER, J. P. 2007 Preliminary investigation of impulsively blocked pipe flow. In *Proceedings of 16th Australasian Fluid Mechanics Conference, Gold Coast, 2007*.

SCHLICHTING, H. 1979 *Boundary-Layer Theory*. McGraw-Hill.

SEED, W. A. & WOOD, N. B. 1971 Velocity patterns in the aorta. *Cardio. Res.* **5**, 319–330.

SENGI, K., UEDA, Y., NISHIHARA, K., KNISLEY, C. W., SASAKI, Y. & IGUCHI, M. 2011 Effect of repeatedly imposed acceleration on the transition to turbulence in transient circular pipe flow. *J. Japan Soc. Exp. Mech.* **11**, SS31–SS36.

SHEN, J. 1997 Efficient spectral-Galerkin methods in polar and cylindrical geometries. *SIAM J. Sci. Comput.* **18** (6), 1583–1604.

SHEN, J. 2000 Stable and efficient spectral methods in unbounded domains using Laguerre functions. *SIAM J. Numer Anal.* **38** (4), 1113–1133.

SUGAWARA, M. 1987 Blood flow in the heart and large vessels. *Med. Prog. Tech.* **12**, 65–76.

TREFETHEN, L. N. 2000 *Spectral Methods in* MATLAB. SIAM.

VARDY, A. E. & BROWN, J. 1995 Transient, turbulent, smooth pipe friction. *J. Hydraul. Res.* **33**, 435–456.

WEINBAUM, S. & PARKER, K. H. 1975 The laminar decay of suddenly blocked channel and pipe flows. *J. Fluid Mech.* **69**, 729–752.